

FULL PAPER

Open Access

Mechanical and hydraulic behavior of a rock fracture under shear deformation

Satoshi Nishiyama^{1*}, Yuzo Ohnishi², Hisao Ito³ and Takao Yano⁴

Abstract

With regard to crystalline rock that constitutes deep geology, attempts have been made to explore its hydraulic characteristics by focusing on the network of numerous fractures within. As the hydraulic characteristics of a rock are the accumulation of hydraulic characteristics of each fracture, it is necessary to develop the hydraulic model of a single fracture to predict the large-scale hydraulic behavior. To this end, a simultaneous permeability and shear test device is developed, and shear-flow coupling tests are conducted on specimens having fractures with varied levels of surface roughness in the constant normal stiffness conditions. The results show that the permeability characteristics in the relation between shear displacement and transmissivity change greatly at the point where the stress path reaches the Mohr-Coulomb failure curve. It is also found that there exists a range in which transmissivity is not proportional to the cube of mechanical aperture width, which seems to be because of the occurrence of channeling phenomenon at small mechanical aperture widths. This channeling flow disappears with increasing shear and is transformed into a uniform flow. We develop a simulation technique to evaluate the macroscopic permeability characteristics by the lattice gas cellular automaton method, considering the microstructure of fracture, namely the fracture surface roughness. With this technique, it is shown that the formation of the Hagen-Poiseuille flow is affected by the fracture microstructure under shear, which as a result determines the relationship between the mechanical aperture width and transmissivity.

Keywords: Shear-flow coupling test; Constant normal stiffness; Fracture surface roughness; Mohr-Coulomb failure; Lattice gas cellular automaton; Modified cubic law; Hagen-Poiseuille flow

Background

In fractured rock such as granite in the Earth's crust, the hydraulic characteristics are dominated by the inherent fluid flows through fractures within the dense matrix. Research has been performed regarding the actual flow speed of groundwater inside such fractures, and regarding the hydraulic characteristics of rock by focusing on the network of fractures. As the hydraulic characteristics of rock are the accumulation of the hydraulic characteristics of each fracture, it is necessary to develop a hydraulic model of a single fracture to predict a large-scale hydraulic behavior (e.g., Raven and Gale 1985; Yeo et al. 1998; Chen et al. 2000; Olsson and Barton 2001; Kim and Inoue 2003; Watanabe et al. 2008; Chen et al. 2009; Watanabe et al. 2009). When a shear displacement takes place in a rock

fracture having rough surfaces, it may cause significant changes in the pore structure (e.g., Mitsui et al. 2012). In terms of an evaluation technique for permeability characteristics, research has been conducted in order to confirm that the permeability through the fracture increases in proportion to the cube of the mechanical aperture width, namely the cubic law flow model (e.g., Brown 1987; Oron and Berkowitz 1998; Brush and Thomson 2003; Konzuk and Kueper 2004; Qian et al. 2011a). Furthermore, research conducted so far has shown that non-cubic law flows in complex fracture models may be caused by the heterogeneity of fractured media (e.g., Zimmerman et al. 1992; Qian et al. 2006; Qian et al. 2012). However, there has been no research that has dealt with how each fracture's permeability characteristics (such as the cubic law flow model) can be expressed in the presence of shear deformations. This study develops a hydraulic model to represent the permeability characteristics inside a single fracture under shear, through shear-flow coupling

* Correspondence: nishiyama.satoshi@okayama-u.ac.jp

¹Graduate School of Environmental and Life Science, Okayama University, Tsushima-naka 3-1-1 Okayama 700-8530, Japan

Full list of author information is available at the end of the article

experiments on fractured specimens. In general, the shear-flow coupling testing on rock fractures is performed under either constant normal load conditions (CNL tests), or constant normal stiffness conditions (CNS tests) (e.g., Mourzenko et al. 1995; Brown et al. 1998; Nicholl and Detwiler 2001; Auradou 2009). We need to estimate strength parameters c and ϕ to understand the shear behavior of rock fractures. CNL tests are usually performed to calculate these strength parameters, at various levels of normal stress. Alternatively, when using CNS tests, it is possible to describe the failure curve of a specimen by obtaining the strength parameters c and ϕ with a single specimen, avoiding the need to prepare many specimens. In this study, we carried out CNS tests combined with permeability tests to show that the hydraulic model of each fracture (cubic or non-cubic model) constituting a fracture network can be expressed to account for both the shear state and changes in the pore structure.

Furthermore, this study sheds light on the mechanism that explains the hydraulic model through simulation. For the simulation of groundwater behavior inside a fracture in particular, it is necessary to develop a methodology to directly incorporate the fracture's physical structure data such as the measured surface profiles and aperture status of the fracture. The lattice gas automaton (LGA) method, which is based on the cellular automata theory, is adopted here to serve this purpose (e.g., Frisch et al. 1987; Pot and Karapiperis 2000; Pot and Genty 2007). Using this technique, we develop a methodology for predicting the behavior of rock that is affected by changes in stress fields.

Methods

Outline of permeability-shear tests

This section focuses on fracture surface profiles, in order to examine the relationship between the permeability behavior of a fracture under shear and its microstructure. We conducted shear-flow coupling tests on specimens having a single fracture.

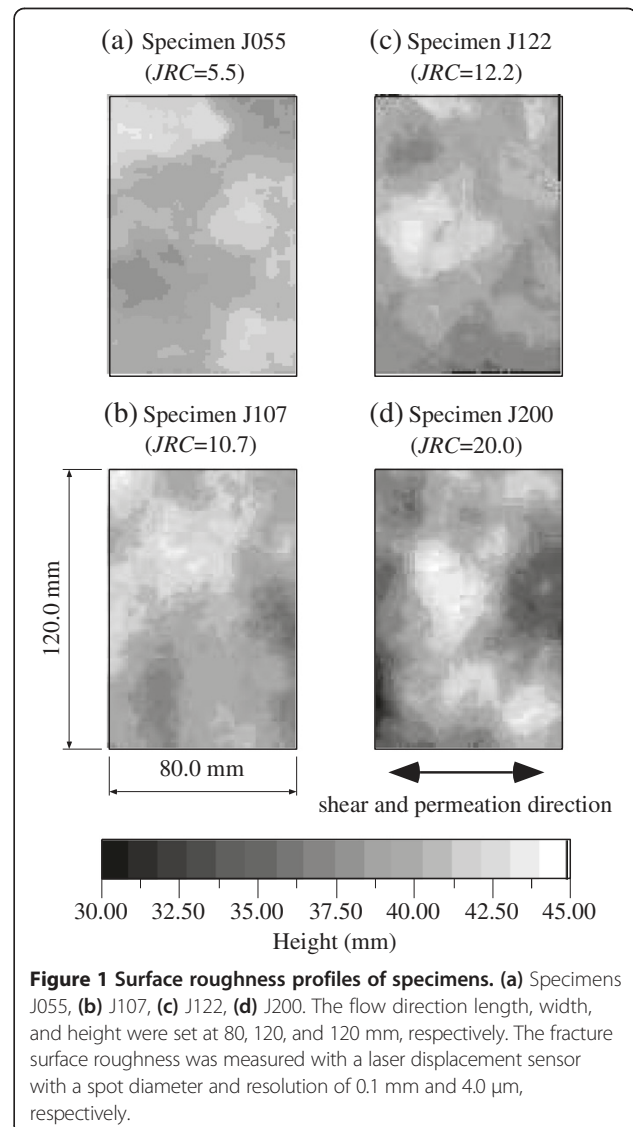
Specimens

The specimens are made of mortar, with uniaxial compressive strength of 29.98 MPa, cast with the surface roughness profiles of natural rock fractures. Cuboid specimens (80.0-mm long \times 120.0-mm wide \times 120.0-mm high), with single fractures 60.0 mm from the bottom, were produced by placing cement mortar (mixture proportions of cement/silica sand #6/distilled water = 1:2:0.65) into a silicon rubber mold formed from a natural rock fracture (Park and Song 2013). The transmissivity of the cement mortar was 5.46×10^{-9} cm²/s. The surface roughness profiles were measured for level differences on a 0.25-mm grid, using a roughness measurement device with a non-contact laser displacement sensor (a spot diameter

of 0.1 mm, featuring a 4.0- μ m high-resolution semiconductor laser as the light source). Figure 1 shows the surface roughness profiles of the specimens used in this study. Fracture roughness is quantified as joint roughness coefficient (JRC), and JRC was determined by a visual comparison of fracture profile measured with standard roughness profile suggested by Barton and Choubey (1977). Using Z2, a parameter that characterizes the roughness profile of fractures proposed by Tse and Cruden (1979), the JRC values in the figure were obtained by applying the Z2-JRC conversion formula proposed by Yu and Vayssade (1991).

Outline of the shear-flow coupling tests

In order to clarify the permeability characteristics of rock fractures under shear, this study incorporated permeability and cutoff mechanisms into the conventional shear-flow



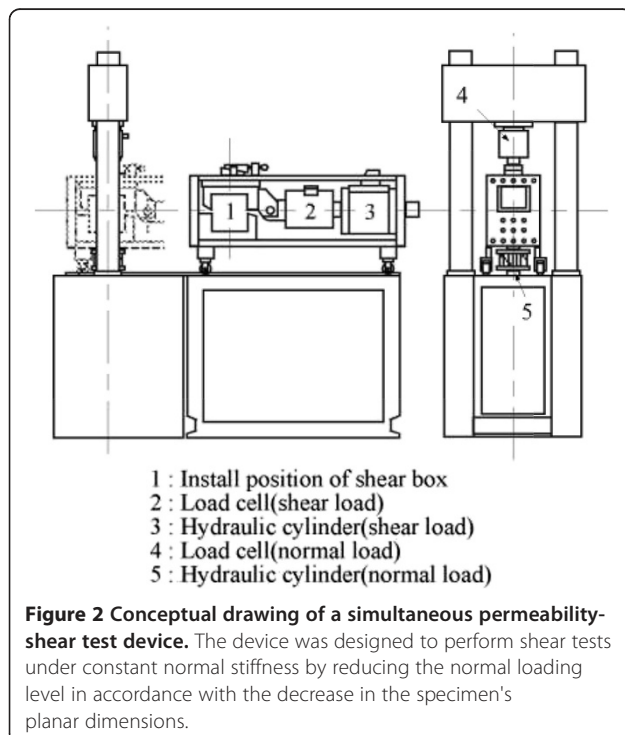
coupling test device to enable the falling head permeability tests. The device was further modified to allow the inflow and measurement of tracers. The parts of the device used for shear-flow coupling testing and for permeability testing are called the 'Shearing device part' and 'Permeability mechanism part,' respectively (Barla et al. 2010; Esaki et al. 1999; Jiang et al. 2004; Giger et al. 2011; Qian et al. 2011b).

Shearing device part

A schematic drawing of the shearing device part is given in Figure 2. A feedback control servo system allows the application of shear and vertical loads, maintaining a vertical stress while shearing the specimen at a constant speed of 0.1 mm/min. With these functions, the device is designed to perform CNS tests by reducing the normal loading level in accordance with the decreases in the specimen's planar dimensions to keep the normal stiffness constant. The vertical displacement is measured with differential displacement transducers, which are directly installed at two positions on the specimen. The average value of the measurements taken at the two positions is used for calculating the mechanical aperture width. Shear displacements are also directly measured at one position on the specimen.

Permeability mechanism part

The permeability mechanism part consists of a cutoff mechanism incorporated into the 'cassette type' shear box, and the permeability mechanism itself, which is



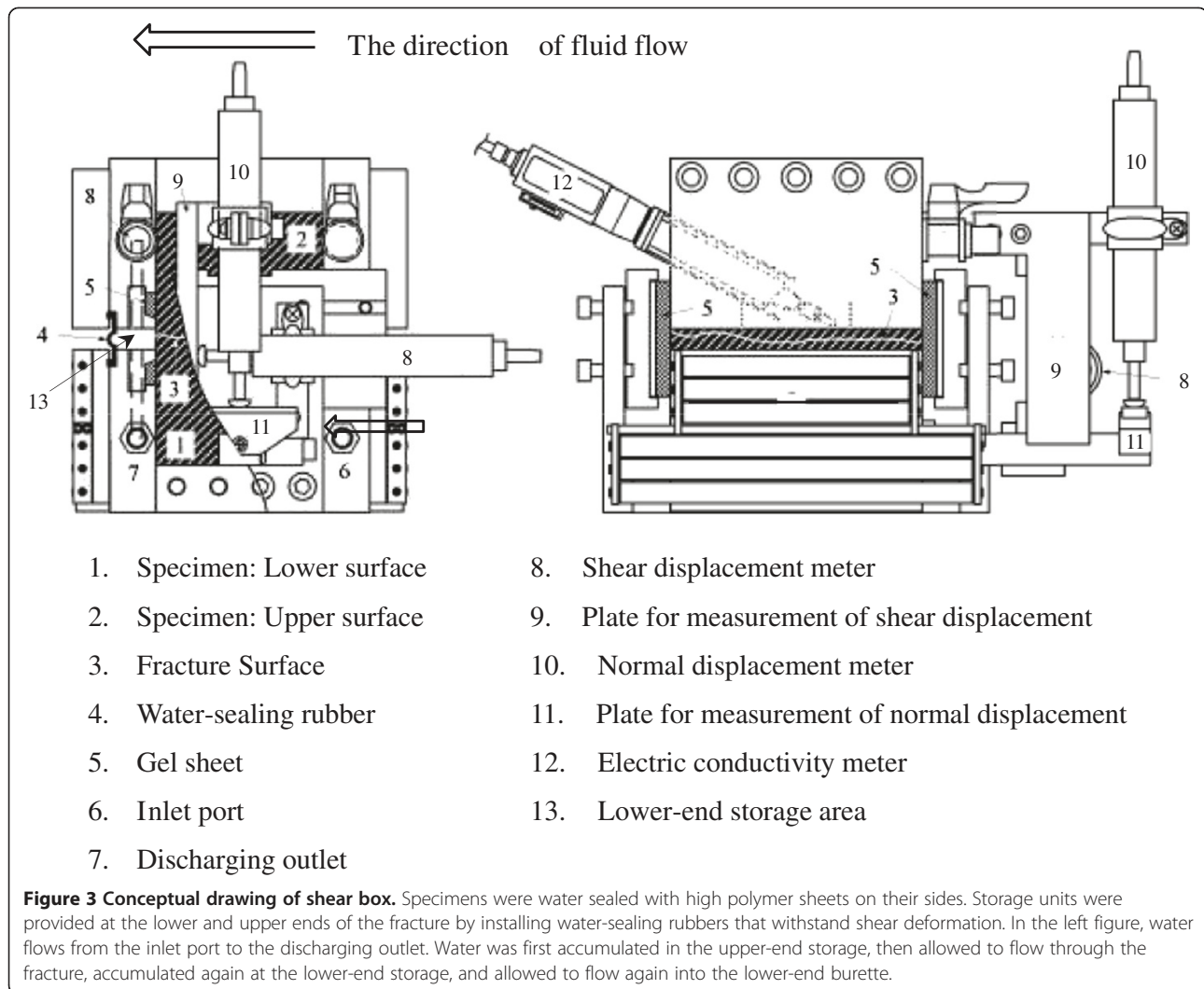
provided by connecting the box shear test device to an upper stream tank, a tracer tank, and a lower-end burette for the falling head permeability tests. With this configuration, one-way flows can be created inside the fracture under shear. As shown in Figure 3, the shear box has a fluid cutoff structure, with an extremely soft and deformable polymer material called 'gel sheets' on the specimen sides. At the upper and lower ends of the fracture, storage areas are provided using cutoff rubbers specially shaped to withstand shear deformation. Fluid flowing down to the shear box is stored in the upper-end storage area, infiltrated through the fracture, and then, it is stopped at the lower-end storage area to flow down to the lower tank or to the lower-end burette. Distilled water is used as the fluid. Because the viscosity of a fluid changes with a change in temperature, the water temperature is kept constant at 20°C throughout the tests.

Two electric conductivity cells are installed at the upper and lower ends of the shear box such that the sensor heads are at the upper-end and lower-end storage areas, and the gaps between the box and cells is sealed with rubber. In the tracer tests, the concentration of the tracer discharge is obtained by measuring the electric conductivity R during the replacement of fluid inside the fracture. The electric conductivity cells used here have a measurement range and accuracy of 0.1 mS/m to 10.0 S/m and 0.1 mS/m, respectively, use platinized electrodes as sensors, and allow the detection of electric conductivity by the two-electrode alternating current method. The tracer is a saline solution with an electric conductivity of 9.5 S/m that has the same viscosity as water, and is designed to measure the change of concentration with time at the upper- and lower-end storage areas.

Test methods and conditions

Shear-flow coupling tests were performed through shear displacement control at a shearing speed of 0.1 mm/min. Permeability tests were performed by pausing the shearing process in order to take measurements at a constant value of shear displacement u , then restarting the shearing process until the next measurement point, continuing in this manner up to a maximum of $u = 3.0$ mm. Before beginning the shearing process, a loading/unloading process (stiffness testing) was repeated up to three times, with a normal stress σ_v value that would not damage the surface roughness of the fracture (from 0.25 up to 4.0 MPa at intervals of 1.0 MPa/min). The tests had originally been intended to be conducted at laboratories to obtain the fracture's normal stiffness k_n . Here, however, the purpose of conducting these tests was to set the same initial conditions, and also to calculate the initial aperture width through the improvement of fracture interlocking.

First, in order to examine how the surface roughness of a fracture would affect its permeability characteristics,



three types of specimens having different surface roughness profiles were prepared (Specimens J055, J107, and J200), which have JRC values of 5.5, 10.7, and 20.0, respectively. In the CNS tests, the hydraulic gradient I was set at a constant value of 12.5 and initial normal stress σ_{v0} and normal stiffness K_v at 1.0 MPa and 10.0 GPa/m, respectively; the CNS and NL tests were conducted. 'NL' refers to the tests performed at constant normal load conditions, in order to examine the permeability characteristics as the mechanical fracture aperture width b_m value becomes smaller.

Next, in order to examine how K_v would affect the fracture permeability, the CNS tests were conducted on a specimen with the same roughness profile (Specimen J055, JRC = 5.5), using constant I and σ_v values of 12.5 and 1.0 MPa, respectively, while setting the values of K_v at 10.0, 30.0, and 50.0 GPa/m.

In general, the transmissivity T is used to represent fracture permeability characteristics when the flow inside

fractures is assumed to follow Darcy's law. T is given by the following

$$T = \frac{Q}{Iw} \quad (1)$$

where Q is the flow rate per unit time, I is hydraulic gradient, and w is the permeation width.

Before applying shear, the process of vertical stress loading and unloading is repeated (up to 4.0 MPa at 1.0 MPa/min) so as not to alter the surface roughness. When the vertical loading-displacement curve starts to follow the same path, it is considered that the upper and lower surfaces of the specimen have interlocked well enough to be ready for the shear test. Assuming that at this stage any further application of stress will no longer affect the status of the aperture, the initial aperture width is defined as the fracture aperture width before commencing the shear test and is derived from the relation between the

change in vertical stress and displacement. The mechanical aperture width b_m is defined as the value obtained by adding the experimentally obtained vertical displacement to the initial aperture width (Bandis et al. 1983; Barton et al. 1985).

In the basic cubic law flow model, the fractures are modeled as parallel plates, and the flow is assumed to be laminar. The cubic law assumes that the average flow rate of a fracture is proportional to the cube of aperture width, which can be derived from the Navier-Stokes dynamic equation and is formulated as shown in Equations 2 and 3, based on the following three assumptions:

- 1) The flow is constant and of the Hagen-Poiseuille type.
- 2) As compared with the speed of flow in the direction parallel to the plate, the speed of flow in the direction orthogonal to the plate is negligible.
- 3) The changes in the speed of flow in the direction parallel to the plate are negligibly small, as compared with those in the direction orthogonal to the plate.

$$\frac{Q}{\Delta H} = C \cdot b^3 \quad (2)$$

$$C = \frac{g}{12\nu} \cdot \frac{w}{l} \quad (3)$$

where Q is the flow rate, ΔH is the head difference, b is the aperture width, g is the gravity acceleration, ν is the dynamic viscosity coefficient of the permeating fluid, w is the specimen width in the direction orthogonal to permeation direction, and l is the specimen length in the permeation direction.

With regard to the applicability of the cubic law model, numerous researches have been performed. In the case of smooth fractures, Witherspoon et al. (1980) proposed the following modified cubic law model considering the impacts of rock's surface roughness profile using a resistance coefficient f_c , which is a deviation from the cubic law model that assumes parallel plates:

$$Q \frac{1}{f_c} \frac{g}{12\nu} w l b^3 \quad (4)$$

Here, f_c represents how the flow inside fractures is affected by the roughness profile of the surface, modifying the cubic law assumption of parallel plates. The closer the f_c value is to one, the smaller the extent of the flow being affected by the fracture, and the smaller the decrease in Q from the value for flow between parallel plates. In this study, the modified cubic law model given by Equation 4 is used for the flow in fractures when the cubic law model is discussed in terms of b_m (Vilarrasa et al. 2011; Xiong et al. 2011).

Results and discussion

Influences of JRC of fracture on the mechanical and permeability characteristics

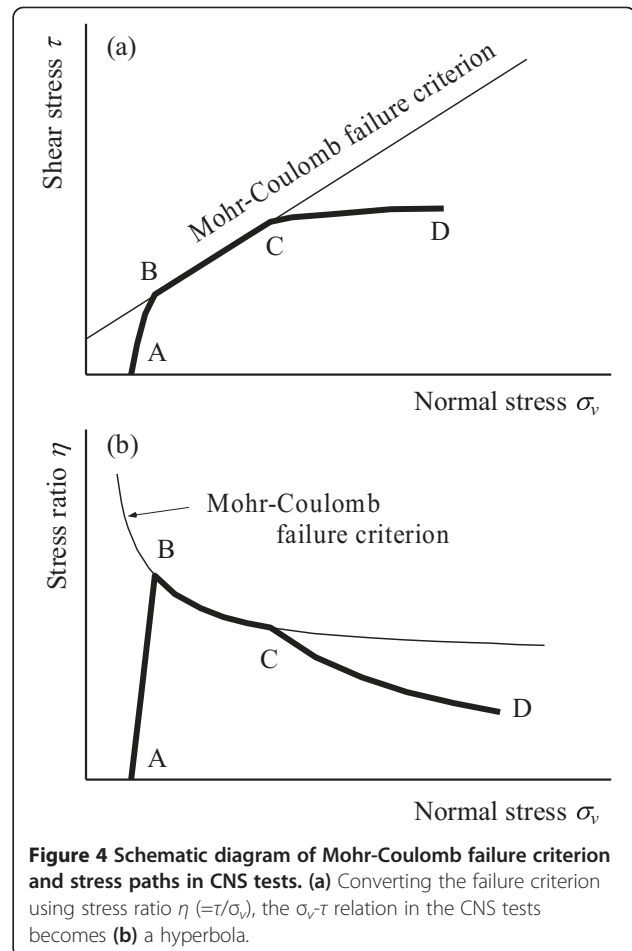
The mechanical characteristics of CNS tests are described, before going on to the permeability characteristics. Assuming that the shearing behavior of rock fractures follows the Mohr-Coulomb failure criterion, the following equation is given:

$$\tau = c + \sigma_v \tan \phi \quad (5)$$

where τ is the shear strength, σ_v is normal stress, c is apparent cohesion, and ϕ is the internal friction angle. Figure 4 shows the schematic diagram of the relation between the Mohr-Coulomb failure criterion and the τ - σ_v relation in the CNS tests. By converting the failure criterion shown in Figure 4a using stress ratio $\eta (= \tau/\sigma_v)$, the relation becomes a hyperbola, as shown in Equation 5 and Figure 4b:

$$\eta = \frac{c}{\sigma_v} + \tan \phi \quad (6)$$

Therefore, if the measured values are expressed by the τ - σ_v relation, the values of c and ϕ can be predicted



based on the hyperbola's curvature and asymptote, by extracting the B-C hyperbola section, as shown in Figure 4b. The point at which the stress path reaches the failure curve (i.e., the maximum η value or η_p) is denoted by the point 'B' in the figure, and the point 'C' can be specified by the critical normal stress σ_{vc} and critical shear stress τ_{pc} . Thus, it becomes possible to objectively define the B-C section. The stresses σ_{vc} and τ_{pc} are the maximum values that the stress path can migrate to in the Mohr-Coulomb failure criterion.

Figure 5 shows the mechanical behavior observed in CNS tests. Figure 5a,b shows the mechanical characteristic that for a greater JRC value, there is a greater τ and a greater dilation. Figure 5c,d shows the results of applying Equation 6; the applicability of the hyperbola approximation described above is confirmed in Figure 5c, while Figure 5d shows that the stress path accurately represents the Mohr-Coulomb failure criterion, and that the greater the JRC values, the greater the c and ϕ values.

Next, with regard to the applicability of the cubic law model given by Equation 4, Figure 6 shows the b_m - T

relation. The figure also shows the results of NL tests, i.e. the results of the permeability tests where the σ_v value was set to 1.0, 2.0, 4.0, 8.0, and 16.0 MPa (shown by the black mark in the figure). It is found that the T value rapidly increased near the shear displacement u_l that corresponds to the proportional limit shown in Figure 5, and then after η_p showed approximately a linear behavior on both logarithm axes. Thus, it is shown that the application boundary for the modified cubic law model given by Equation 4 is η_p , and the permeability characteristics in the u - T relationship change greatly before and after reaching the Mohr-Coulomb failure curve, regardless of the fracture surface profiles (Mourzenko et al. 1997; Yeo and Ge 2005).

Influents of normal stiffness on the mechanical and permeability characteristics

Described here are the influences of the K_v values that are set in the CNS tests on the mechanical and permeability characteristics of rock fractures. With regard to the mechanical characteristics, Figure 7 shows the mechanical

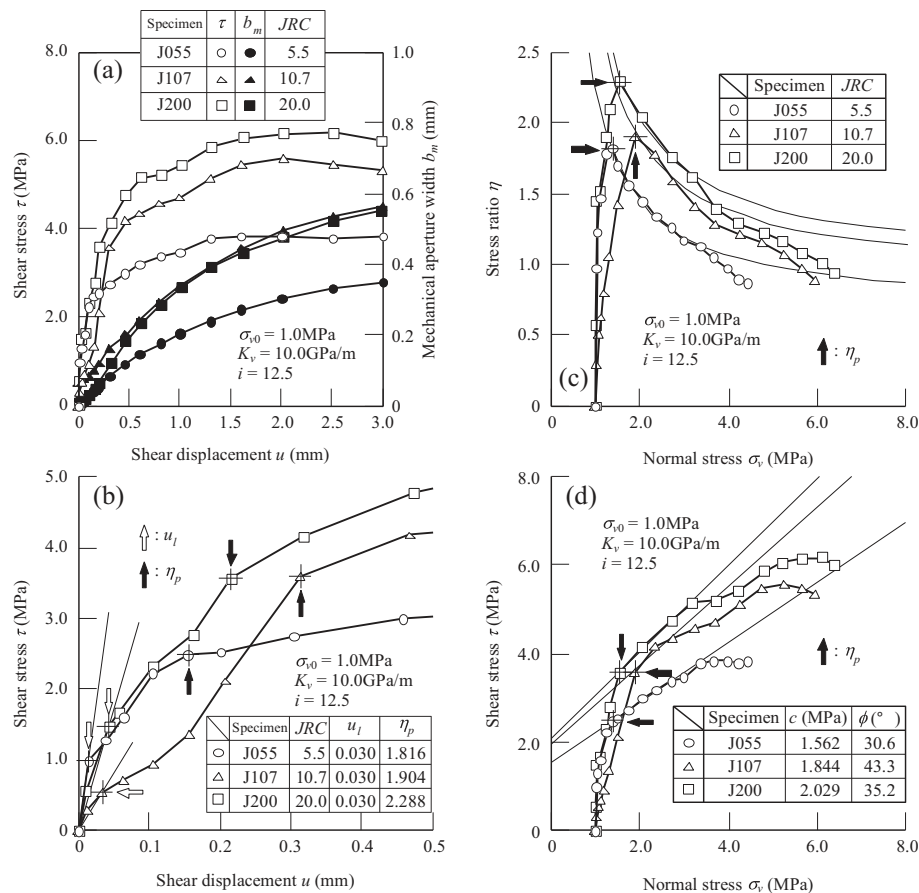


Figure 5 Results of influences of JRC on mechanical behavior in the CNS tests. (a) u - τ , b_m relation; (b) u - τ relation; (c) σ_v - η relation; (d) σ_v - τ relation. The stress path well represents the Mohr-Coulomb failure criterion.

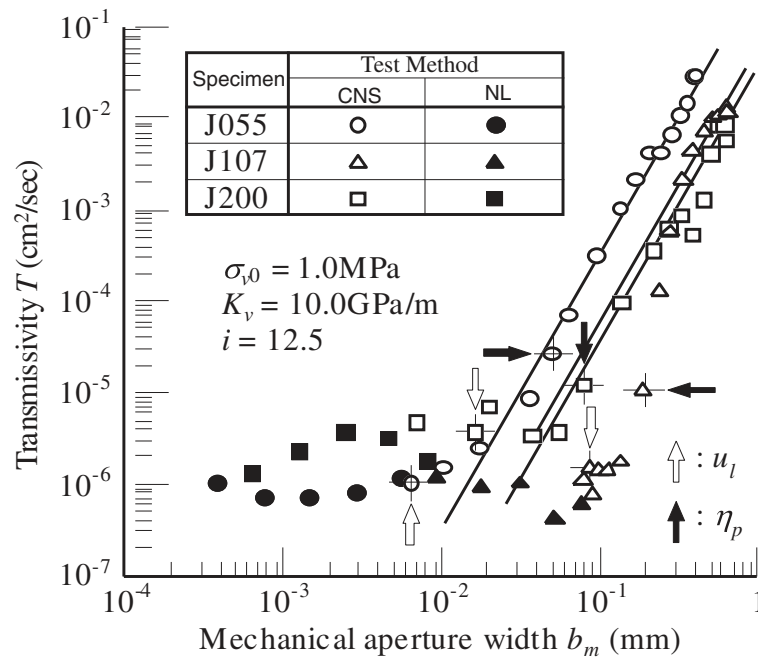


Figure 6 Results of influences of JRC on b_m - T relation in the CNS tests. The permeability characteristics in the u - T relations change greatly before and after reaching the Mohr-Coulomb failure curve. In the b_m - T relation, where b_m was small, there exists a range in which T was not proportional to the cube of b_m . This seemed to be caused by the occurrence of channeling phenomenon at small b_m values.

behavior observed in the CNS tests. The figure also shows the results of the NL tests. Because the value of σ_v is constant in the conventional CNL tests, regardless of any changes in v , it is possible to compare the results of the NL tests by assuming they are equivalent to a CNS test with a K_v value of 0. Figure 7a shows the relation between u , τ , and b_m . Figure 7b is an enlarged view of the u - τ relation. Note that $\sigma_{v0} = 1.0$ MPa. The u - τ - b_m relation in Figure 7a, b shows that the greater the value of K_v , the greater the value of τ , and the u - b_m relation shows that the greater the value of K_v , the lower the value of b_m . Figure 7c shows the results of applying Equation 6, which confirms the applicability of the hyperbola approximation method. Figure 7d is the stress path. When the values of c and ϕ obtained by the hyperbola method are applied, it is shown that while c is highly dependent on the K_v value, ϕ is approximately independent.

With regard to the permeability characteristics, Figure 8a shows the u - T relation. It is also shown here that the T value rapidly increased near u_l in Figure 7, and after, η_p showed a linear behavior on both logarithm axes. Figure 8b shows the relation between b_m and T . The figure also shows the results of the NL tests, which are the permeability tests where σ_v values were set at 1.0, 1.5, 2.0, and 4.0 MPa (denoted by the black marks in the figure). The figure confirms that the smaller the b_m value, the larger the deviation from the cubic law model and that the value η_p shown in Figure 7 is the boundary where the modified

cubic law model given by Equation 4 is found to be accurate in all specimens. It is also observed that where the fracture profiles are the same, similar permeability characteristics are observed at large and small b_m values, regardless of any changes in the normal stiffness.

Results in the tracer tests

In the previous section, η_p shown in Figures 6 and 8 is the boundary of the region where the cubic law model is accurate. The reason for the large deviation from the cubic law model can also be found in the tracer tests. Preliminary tracer tests were conducted on an acrylic specimen with a circular hole, 4.0 mm in diameter and 80.0 mm in length. This acrylic specimen had a uniform pore structure in the permeation direction, where permeation and substance migration occurred. The results of the tracer tests with this acrylic specimen were compared with those with complex pore structure fractures that had the same permeation cross section area as the 4.0-mm-diameter circular hole. As shown in Figure 9, the t - R relationships at the entrance and exit were found to be parallel to each other in the pipe model. For fractures with complex wall profiles, there is a time delay in the substance migration curve. The figure shows that with the parallel plates, the time needed for the injected fluid to reach the exit is constant, while there is a delay in the time needed for the fluid flowing through the void created by the fracture to reach the exit, depending on

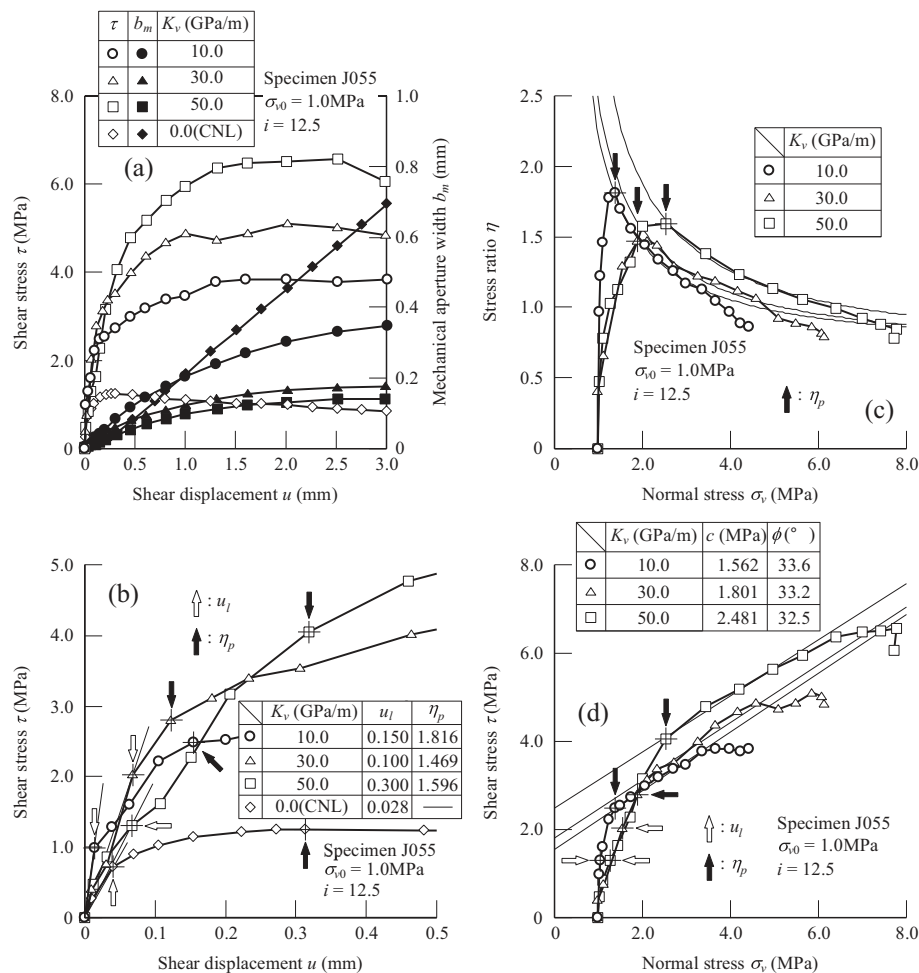


Figure 7 Influences of K_v on mechanical behavior in the CNS tests. (a) $u-\tau, b_m$ relation; (b) $u-\tau$ relation; (c) $\sigma_v-\eta$ relation; (d) $\sigma_v-\tau$ relation.

which path is taken. As pointed out by Piggott and Elsworth (1993), the complex pore structure triggered local migration of the substance inside the fracture. In other words, selective flows are occurring. Figure 10 shows the changes with time in the electric conductivity for each shear displacement u value. Here again, a delay in the curve is observed at the initial shearing stage in accordance with the progress in the shearing process. Therefore, as mentioned before, the channeling phenomenon is presumed to have had a large influence on rapid changes in permeability characteristics before and after reaching the Mohr-Coulomb failure curve (Qian et al. 2011c).

Simulation of fluid behavior inside the fracture

Principle of lattice gas automaton method

The technique of starting from the conventional adoption of differential equations such as the Navier-Stokes formula or the Reynolds equation, in order to obtain the speed or pressure of the fluid in a continuous body, is limited to the understanding of average characteristics within

the domain (e.g., Zimmerman and Bodvarsson 1996; Zimmerman et al. 2004; Koyama et al. 2006; Cardenas et al. 2007). However, the technique proposed here, which treats the fluid as an assembly of particles and thus a discontinuous body, can express any chaotic behavior created by particle interactions. Furthermore, it allows the consideration of interactions within rock representing fracture profiles, and this is beneficial for the identification of the relationship between the microstructure and hydraulic characteristics of the fracture. The lattice Boltzmann (LB) method, which has the same cellular automata structure as LGA, has also been used for many kinds of simulations of incompressible viscous flows. In the LGA method, particles are represented by binary digits, whereas in the LB method, real numbers are utilized to represent the local ensemble-averaged particle distribution functions and only the kinetic equation for the distribution function is solved (e.g., Madadi and Sahimi 2003; Eker and Akin 2006). The main advantages of the LGA techniques are stability, easy introduction of boundary

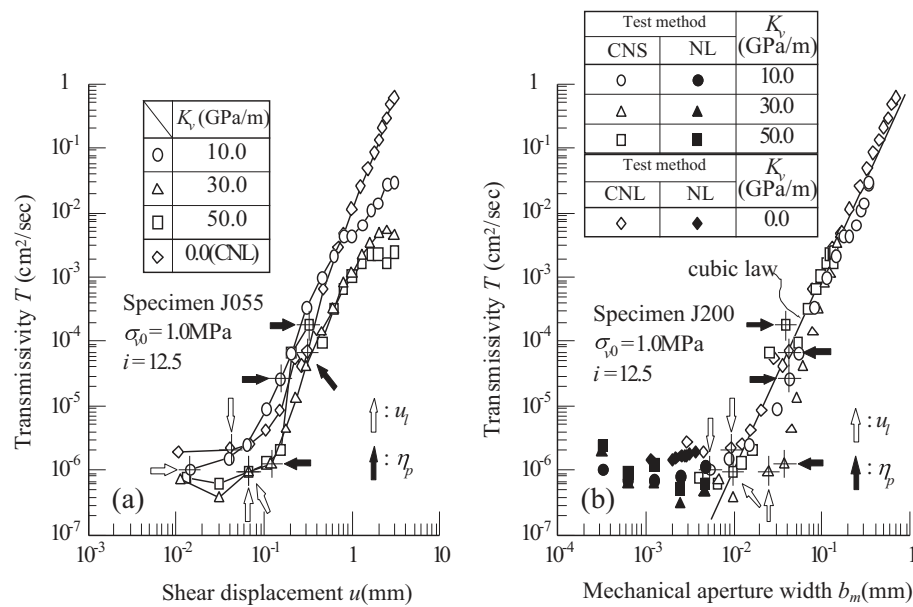


Figure 8 Influences of K_v on permeability characteristics in the CNS tests. (a) u - T relation; (b) b_m - T relation. The permeability characteristics changed greatly before and after reaching the Mohr-Coulomb failure curve regardless of normal stiffness K_v .

conditions, and an effective approach to accurately calculate fluid flow parameters at the microscopic scale, enabling a high-performance computation. Because the LGA method uses Boolean numbers in simulations and is therefore free from round-off error due to floating-point precision, this motivated us to choose the LGA method instead of the LB method.

In the LGA method, the fluid behavior is analyzed in the calculation process as follows:

- 1) Divide the analysis target with the polygon lattice and discretize it.
- 2) Express the fluid as an assembly of virtual particles of unit weight.

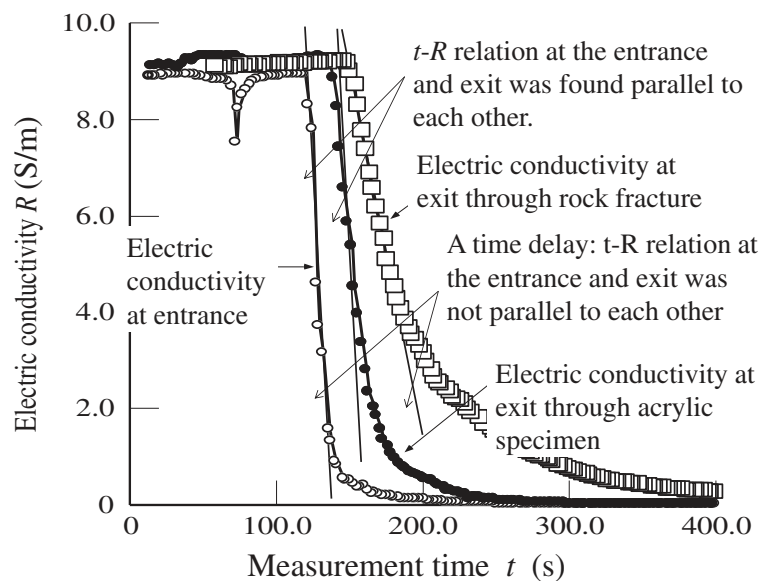


Figure 9 Relation between electric conductivity and measurement time in the tracer tests. The t - R relation at the entrance and exit in the acrylic specimen was found parallel to each other and shows the Hagen-Poiseuille flow. On the other hand, the t - R relation in a rock specimen shows a time delay in the curve because the complex pore structure caused selective flows.

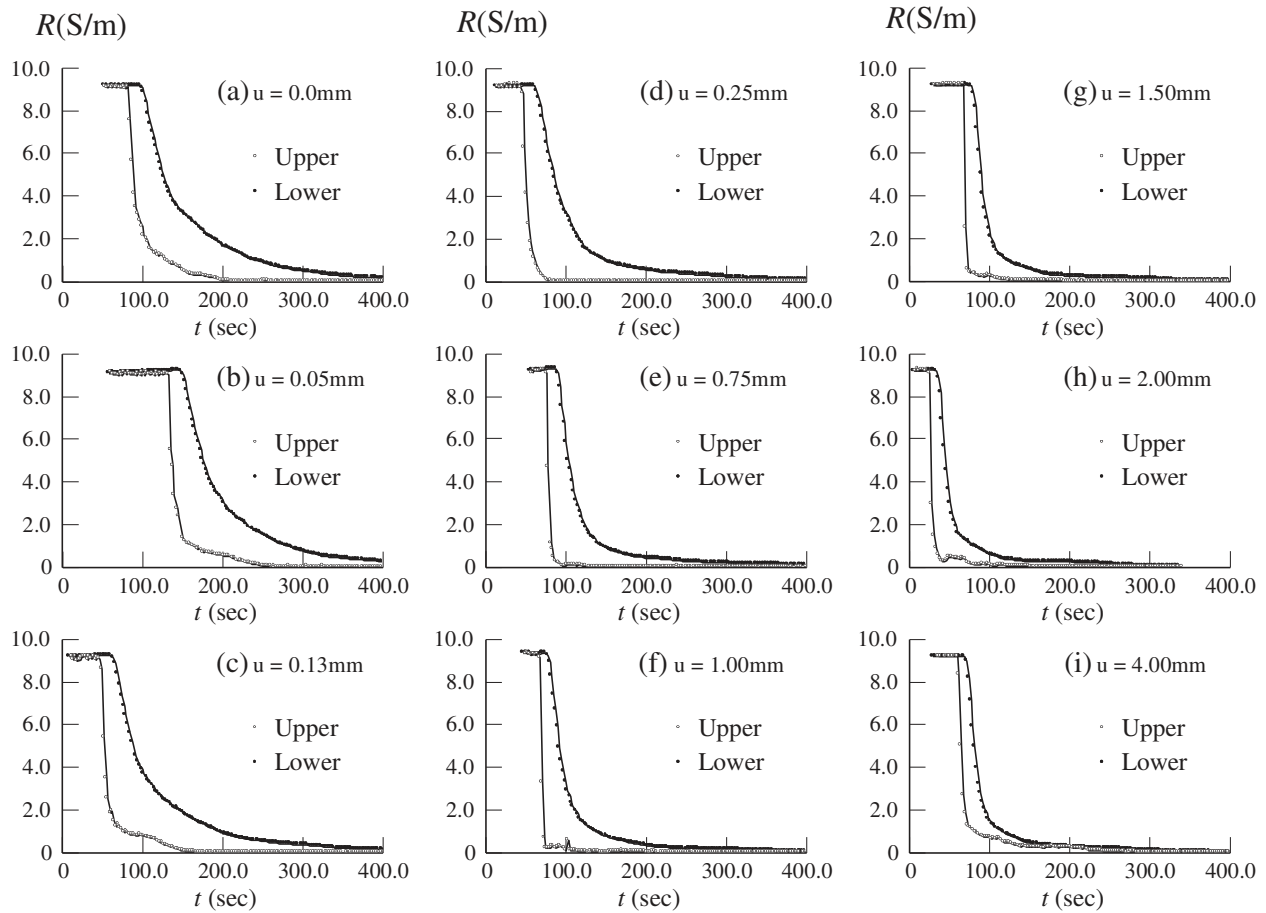


Figure 10 Relation between measurement time t and electric conductivity R in the tracer tests. $u =$ (a) 0.0, (b) 0.05, (c) 0.13, (d) 0.25, (e) 0.75, (f) 1.00, (g) 1.50, (h) 2.00, (i) 4.00 mm. The vertical axis of each graph is the electric conductivity (S/m).

- 3) Allocate the virtual particles on the lattice points. At each lattice point, there should be only one particle, which has a certain speed and direction at a certain time.
- 4) Let the particles migrate, restricting them to the lattice lines. Each particle migrates to the closest lattice point at each discrete time step. During this process, it respects collision with other particles and scattering. The collisions are performed according to the conservation of mass and momentum.

In this study, a three-dimensional projection of four-dimensional face-centered-hyper-cubic (FCHC) lattice is used to discretize the space, as shown in Figure 11. The FCHC lattice consists of lattices that connect neighboring points in 24 directions, each centered around (0,0,0,0). Thus, the state of lattice point $n(r, t) = \{n_i(r, t); i = 1, 2, \dots, b\}$ is expressed by $b = 24$ bits, and the particle can go to neighboring points in 24 directions. Here, the affected neighborhood is set at 0, meaning that the collision and scattering of a particle are only affected by the state at the

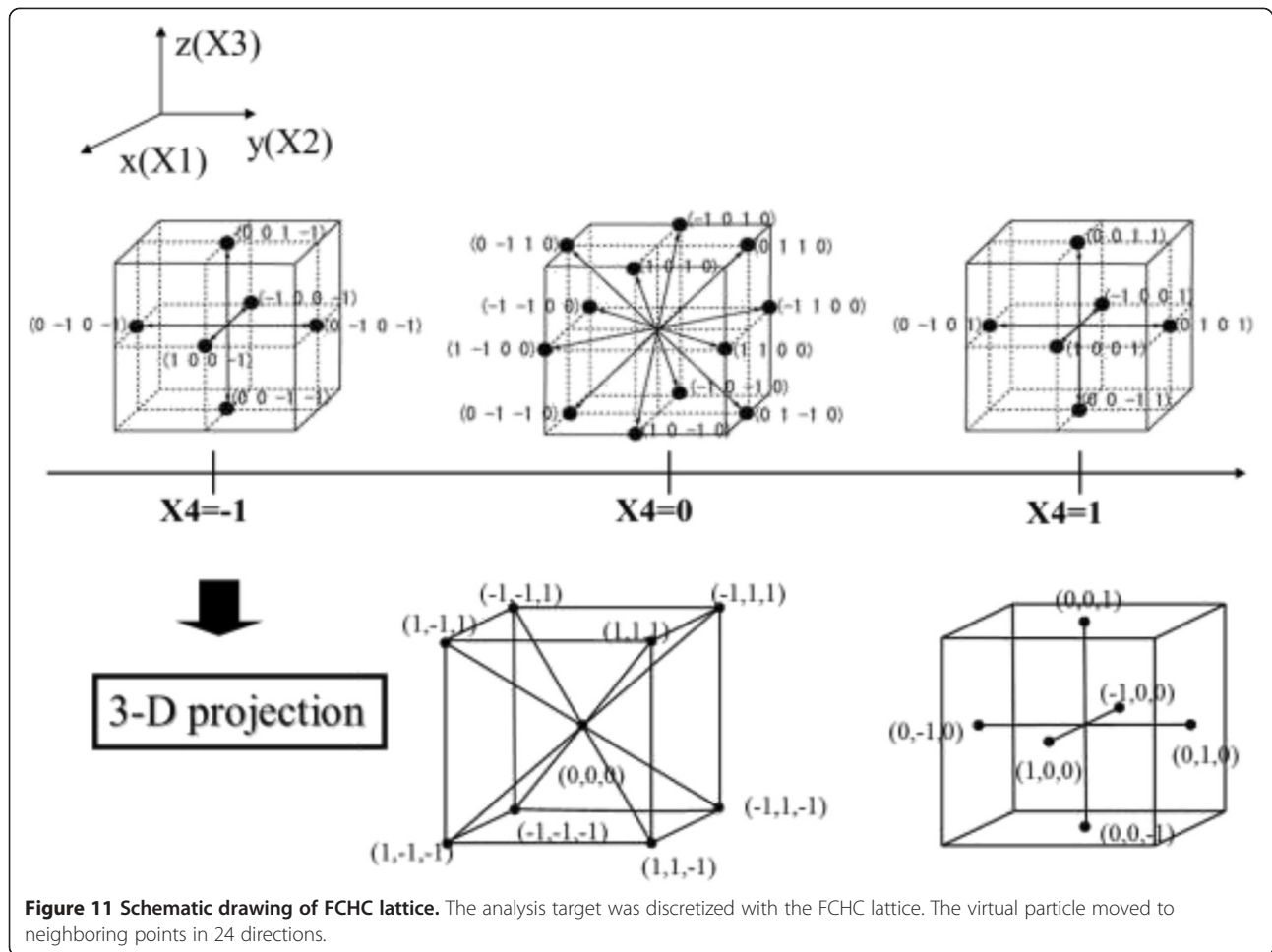
point where the particle is present. As shown in the figure, the four-dimensional axes are denoted by X_1, X_2, X_3 , and X_4 . When projecting onto a three-dimensional space, the X_1, X_2 , and X_3 axes correspond to X, Y , and Z axes, while the X_4 axis is degenerated.

In the collision process of a particle between time steps t and $t + 1$, assuming that c_i is a vector of the lattice line between lattice point r and the neighboring point, the mass and momentum conservation laws are given by Equations 7 and 8, respectively:

$$\sum_i n_i(t + 1, r + c_i) = \sum_i n_i(t, r) \quad (7)$$

$$\sum_i c_i \cdot n_i(t + 1, r + c_i) = \sum_i c_i \cdot n_i(t, r) \quad (8)$$

c_i is the particle's migration speed in the i direction. Using a function Δ_i to represent the collision process, the above equation can be written as Equation 9.



$$n_i(t+1, r+c_i) = n_i(t, r) + \Delta_i \quad (9)$$

In this study, the particle-fracture wall collision is expressed by the combination of slip and non-slip conditions. The non-slip condition represents cases where a particle is bounced back in the incoming direction on the wall. The non-slip condition on the fractured wall in the X_1 , X_2 , and X_3 directions is given by Equation 10 below:

$$\sum_i c_i \cdot n_i(r, t+1) = -\sum_i c_i \cdot n_i(r, t) \quad (10)$$

This is the boundary condition in which the flow speed on the wall becomes zero at the average time. For migration in the X_4 direction, an incident particle on the wall is assumed to undergo specular reflection, the slip condition given by Equation 11 below is adopted:

$$\sum_i c_i \cdot n_i(r, t+1) = \sum_i c_i \cdot n_i(r, t) \quad (11)$$

With these equations, the complex fluid-fracture interactions are represented by the collisions of virtual particles and fracture walls.

LGA simulation developed in this study

Since the LGA method is designed to track the collision and scattering of particles, it is impossible to set the hydraulic boundary condition on the positive side to be a hydraulic gradient. In particular, there is no pressure difference between the upper and lower streams when a particle collides with a fracture wall in the fluid flow direction. Furthermore, when injecting particles from outside the analytical model to eliminate the problem, the mass conservation law becomes invalid inside the model. For solving this problem, if the condition of r being less than one sixth the injected particle density is found to be true in the motion directions of six particles in the flow direction ($+X_i$ direction) in the FCHC lattice, namely $(1,0,0,\pm 1)$, $(1,0,\pm 1,0)$, and $(1,\pm 1,0,0)$, then a particle having the corresponding momentum is added to each particle at the upper end. Then, as shown in Figure 12a, the number of the particles flowing into the model becomes equal to the sum of the number of particles flowing out of the model exit and the number of particles flowing out of the model entrance after bouncing inside the model, satisfying the mass conservation law.

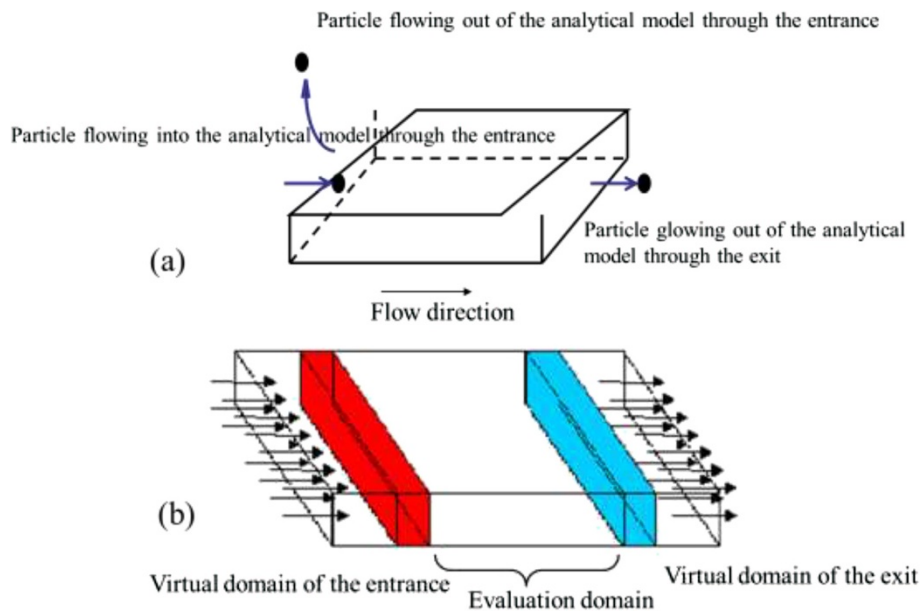


Figure 12 Determination of boundary conditions. (a) The mass conservation law is satisfied by adjusting the number of the particles flowing into and out of the model. The use of an imaginary domain (b) allows virtual particle flow outside the model, evaluating fluid behavior in the region where the influence of interaction with the outside of the fracture cannot reach.

In this case, however, the motion of particle near the model entrance/exit is affected by the fracture's porous structure and the interaction with the flow there, as well as the interaction with the domain outside the model. Thus, as shown in Figure 12b, this study assumes an imaginary domain to allow a virtual particle to flow outside

the model, to perform hydraulic evaluation in the range where the influence of the interaction with the outside of the fracture cannot reach.

The viscosity of the fluid flowing through the fracture is given as a function of the number of particles per lattice point. Injecting particles in the fracture surface in

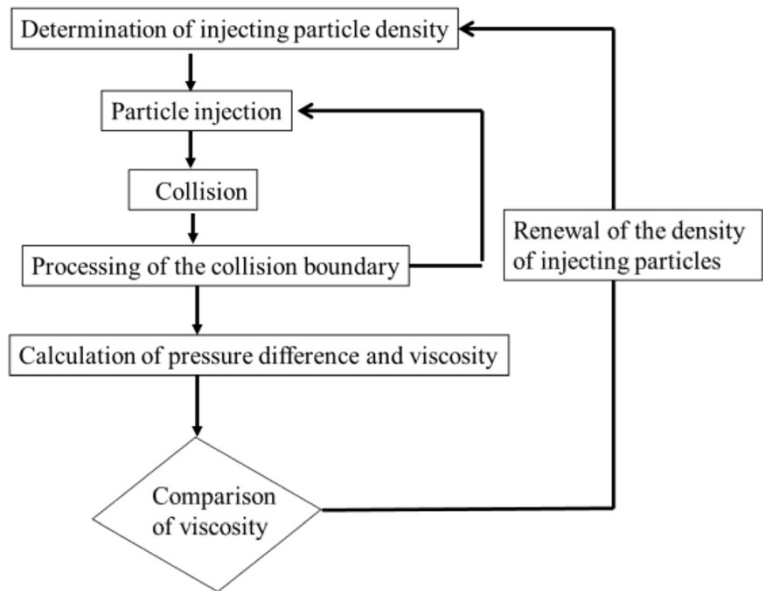


Figure 13 Outline of improved algorithm. The injecting particle density inside the fracture was kept at a constant value by calculating the pressure difference and viscosity simultaneously with the particle collision and scattering. It was possible to keep the fluid viscosity a constant value for various conditions inside the fracture surface by this algorithm.

the LGA method leads to a different density of particles inside the fracture, and as a result, the viscosity ν is found to be different. To avoid this problem, the pressure difference and viscosity are calculated in the process of calculating the particle collision and scattering, as shown in Figure 13. Then, an algorithm is incorporated to keep a constant value for the injecting particle density inside the fracture. In other words, it was made possible to quantitatively evaluate the fluid behavior represented by particle density while keeping the fluid viscosity constant for various conditions inside the fracture surface.

As shown in Figure 14, an example of analyzing the behavior of fluid flowing between two parallel plates in the LGA method is presented here. The aperture between the two parallel plates in the model had 300 lattices in the X direction (flow direction) and 100 in the Y direction (aperture width), with a number that varied between 10 and 30 in the Z direction (aperture thickness direction). The density of the injecting particles at the exit was set at 0, and at the entrance a value of between 0.45 and 0.55, respectively, with 20 lattices in the flow direction in the imaginary domain. In the Z direction, a reflective boundary was assumed in order to produce interactions with the fracture surface, and in the Y direction, there was a cyclic boundary condition.

The particle density within the aperture width was kept at 30. Figure 15a,b shows the values of pressure in the flow direction and flow speed in the Z direction (aperture thickness direction). The former shows a linear decrease, and the latter follows the parabolic distributions. This represents what is known as the Hagen-Poiseuille flow, which is derived from the Navier-Stokes formula. These results prove that the technique developed here allows the evaluation of fluid behavior by the collision/scattering of virtual particles in the microscopic process (Gao and Sharma 1994; Gutfraind and Hansen 1995).

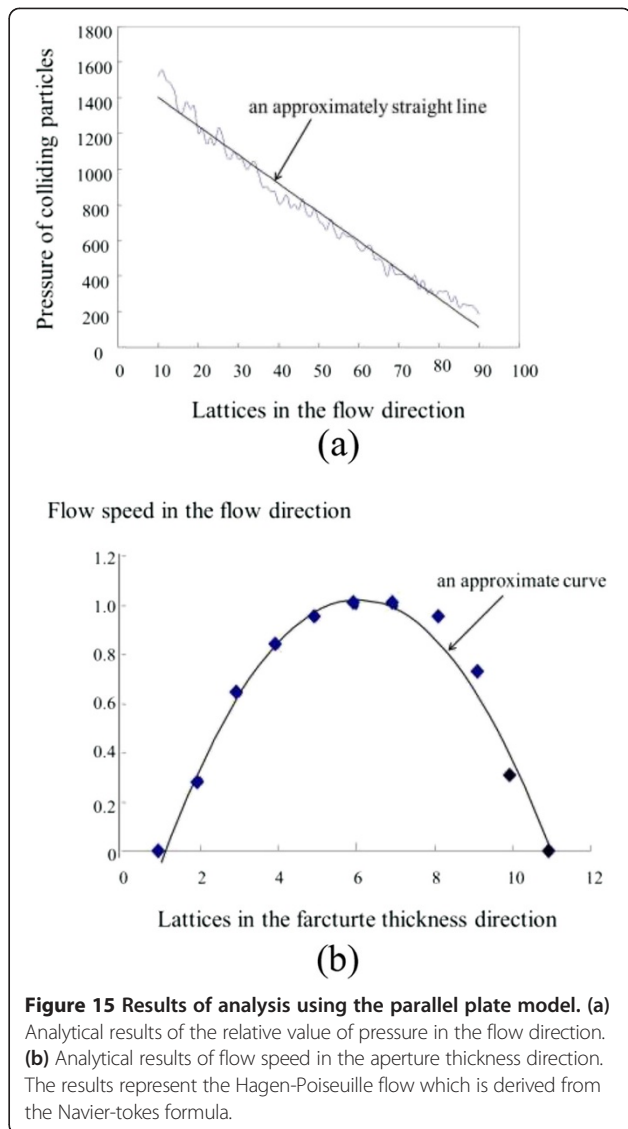


Figure 15 Results of analysis using the parallel plate model. (a) Analytical results of the relative value of pressure in the flow direction. **(b)** Analytical results of flow speed in the aperture thickness direction. The results represent the Hagen-Poiseuille flow which is derived from the Navier-Stokes formula.

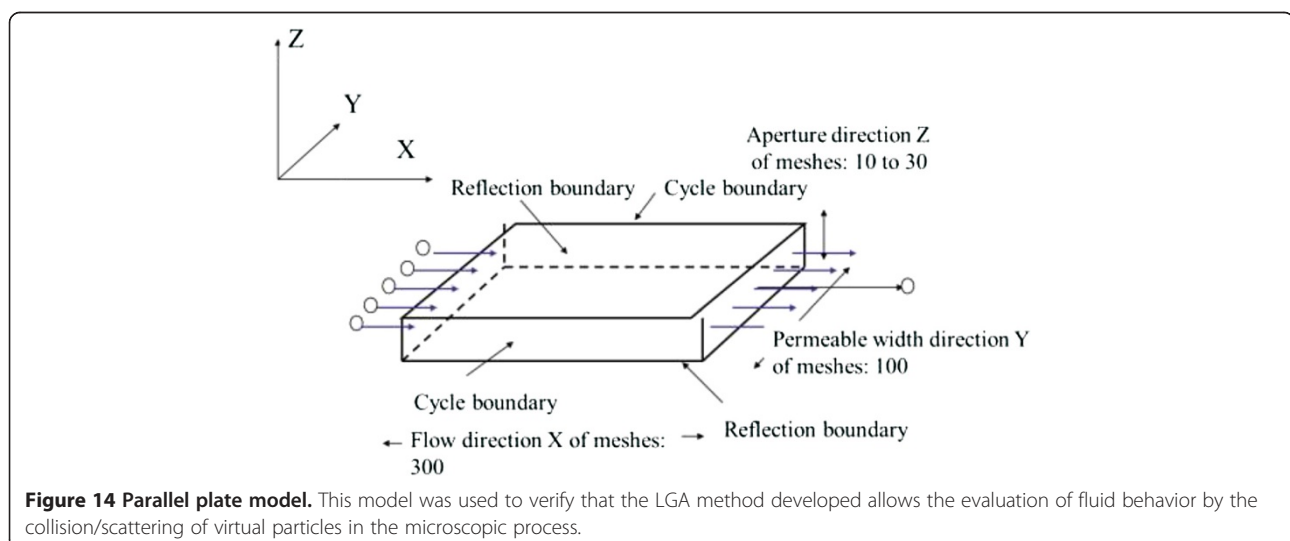


Figure 14 Parallel plate model. This model was used to verify that the LGA method developed allows the evaluation of fluid behavior by the collision/scattering of virtual particles in the microscopic process.

LGA simulation of fluid behavior inside the fracture

An example of simulating the behavior of fluid flowing through the fracture using a model that faithfully represents the surface roughness structure of a specimen with a roughness of JRC 10.7 is shown in Figure 16. The part of the specimen shown here is where fluid flows into the fracture from below towards above at each time. The white areas represent where there are initially no particles. The figures show how the dark blue particles fill the pore inside the fracture at the beginning, and then red particles are injected into the fracture. The most reddish areas represent the highest tracer density. The lower the tracer density, the more bluish the color becomes. The analytical results show that the particles behave so as to avoid the narrow aperture parts, but a low density of tracer particles is found not only in the domains with narrow apertures created by the roughness of the fracture, but also in the vicinity of these domains. This implies that where the aperture width is small, the domains disrupt the fluid flow in a wide area.

Using the aperture elevation distributions obtained in the shear tests, the number of particles on the upper and lower sides of the fracture was tracked for each value of shear displacement. The results are shown in Figure 17. Sheared specimens were extracted for each shear displacement, and a model made by measuring the state of the fracture surface. In this figure also, the ordinal axis represents the number of dark blue particles, which fill the pore at the beginning but are gradually replaced by the injecting particles. Where the shear displacement is large, there is only a small delay occurred in the time needed for substitutions on the

upper and lower streams. However, where the shear displacement is small, there is a larger delay in substitution. This seems to be because of the fact that with a small aperture width, the particles selectively flow through narrow pores and go out of certain pores only as shown in Figure 16, and thus the particle substitution process takes more time. A local flow or 'channeling phenomenon' was produced because the upper and lower specimens were in contact with each other at many locations. When the contact area then became smaller, in accordance with the progress of the shearing process, the flow became uniform and the channeling phenomenon disappeared.

Figure 18 shows a comparison of particle substitution results where fluid is assumed to flow through the fracture at a shear displacement of 0.1 mm, following a Hagen-Poiseuille flow. It is shown that a Hagen-Poiseuille flow corresponds to cases where the shear displacement is large. Given the results described in the previous section, the formation of a Hagen-Poiseuille flow leads to the formation of the cubic law model between the transmissivity and aperture width. The results of shear-flow coupling experiments described in the previous section also showed that the stress field below the proportional limit and the yielding range above it had different transmissivity-aperture width relation. According to the analytical results in the LGA method, the Hagen-Poiseuille flow was difficult to form up to the proportional limit where there was not much dilation development to accompany shear displacement, which as a result prevented the constitution of the cubic law between the transmissivity and aperture width.

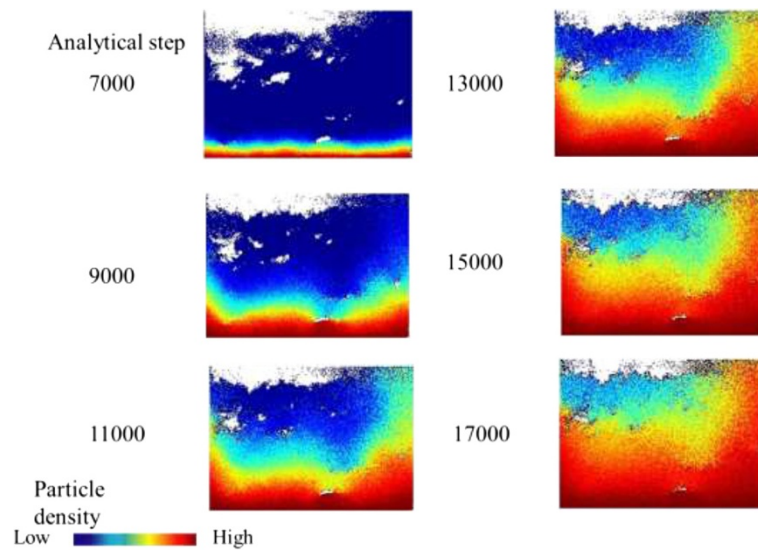


Figure 16 Results of simulation for flow through the fracture. The dark blue particles fill the pore inside the fracture at the beginning, and then red particles are injected into the fracture. Fluid flows into the fracture from below. The red particles flow to avoid the narrow aperture parts and the domains that disrupt fluid flow are found in a wide area.

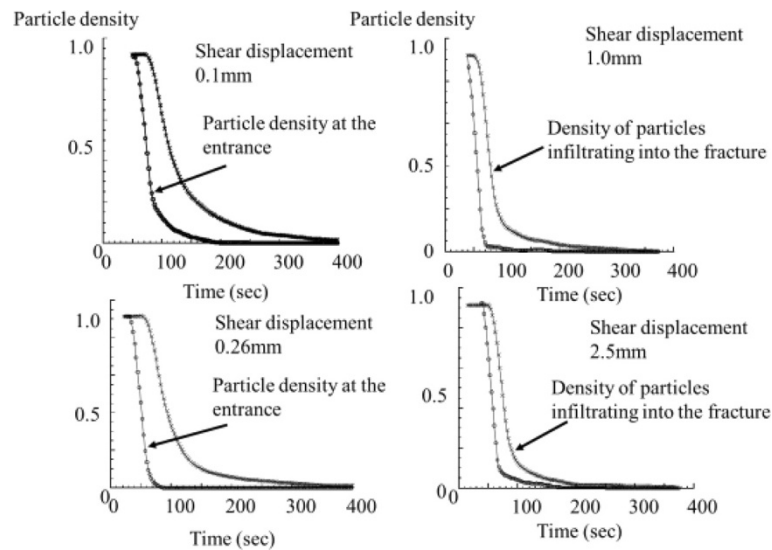


Figure 17 Analytical results of flow through the fracture and shear displacement. Where the shear displacement is small, a delay occurred in the time needed for substitutions in the upper and lower streams.

Conclusions

For clarifying the permeability characteristics of rock fractures, shear-flow coupling tests in constant normal stiffness conditions were conducted in this study. The main insights obtained in this study are as follows:

- (1) According to the u - T relationship, T was found to rapidly increase at u_f . In the CNS tests, it was found that the relation showed linear behavior in both logarithmic axes at η_p and afterwards. This led to

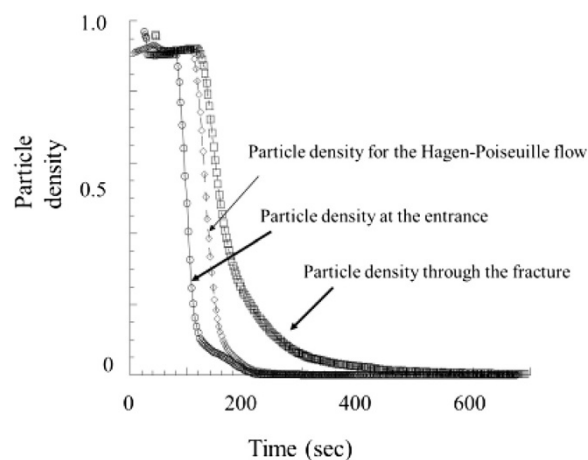


Figure 18 Analytical results of flow through parallel plate and through fracture. The behavior of fluid flowing between two parallel plates follows the Hagen-Poiseuille flow. However, below the proportional limit, it was difficult to form the Hagen-Poiseuille flow, as there was not much dilation development to accompany the shear displacement.

the realization that because η_p is the crossings on the Mohr-Coulomb failure curve, the permeability characteristics represented by the u - T relationship changed greatly before and after reaching the Mohr-Coulomb failure curve.

- (2) Even when the fractures had the same b_m value, they had different permeability characteristics if their pore structures were different.
- (3) There existed a range in which T was not proportional to the cube of b_m where b_m was small in the b_m - T relation. This seems to be caused by the fact that the channeling phenomenon occurred at small b_m values, which disappeared in accordance with the progress of shear process and transformed into a uniform flow.
- (4) The findings (3) above were also confirmed in the tracer tests. A delay in the curve was observed at the initial shearing stage, which confirmed that the flow was gradually transformed into the Hagen-Poiseuille flow in accordance with the progress in shearing process.
- (5) The b_m - T relation of the tests with different K_v using the same specimens was found to follow the same path in accordance with increases in b_m , showing that the same permeability characteristics were observed at large b_m values if the fracture profiles were the same.

Furthermore, taking into account the microstructure of fracture, the LGA method has been developed as an analytical technique for hydraulic behavior using a cellular automaton method to evaluate macroscopic permeability

characteristics. It is then proved that the formation of Hagen-Poiseuille flow is affected by the microstructure of fracture under shear, which as a result determines the relation between the mechanical aperture width and transmissivity.

Competing interests

The authors declare that they have no competing interests.

Authors' contributions

The work presented here was carried out in collaboration between all authors. SN, YO and HI defined the research theme. SN and TY designed methods and experiments, carried out the laboratory experiments, analyzed the data, interpreted the results and wrote the paper. YO and HI co-designed experiments, discussed analyses, interpretation, and presentation. All authors read and approved the final manuscript.

Author details

¹Graduate School of Environmental and Life Science, Okayama University, Tsushima-naka 3-1-1 Okayama 700-8530, Japan. ²Faculty of Civil and Environmental Engineering, Kansai University, Osaka 564-8680, Japan. ³Disaster Prevention Research Institute, Kyoto University, Kyoto 611-0011, Japan. ⁴Graduate School of Engineering, Kyoto University, Kyoto 615-8540, Japan.

Received: 27 February 2014 Accepted: 22 August 2014

Published: 4 September 2014

References

- Auradou H (2009) Influence of wall roughness on the geometrical, mechanical and transport properties of single fractures. *J Phys D* 42:214015, doi: 10.1088/0022-3727/42/21/214015
- Bandis SC, Lumsden AC, Barton NR (1983) Fundamentals of rock joint deformation. *Int J Rock Mech Min Sci Geomesh Abstr* 20(6):249–268
- Barla G, Barla M, Martinotti ME (2010) Development of a new direct shear testing apparatus. *Rock Mech Rock Eng* 43:117–122
- Barton N, Choubey V (1977) The shear strength of rock joints in theory and practice. *Rock Mech* 10:1–54
- Barton N, Bandis S, Bakhtar K (1985) Strength, deformation and conductivity coupling of rock joints. *Int J Rock Mech Min Sci Geomesh Abstr* 22(3):121–140
- Brown SR (1987) Fluid flow through rock joints: the effect of surface roughness. *J Geophys Res* 92(B2):1337–1347
- Brown S, Caprihan A, Hardly R (1998) Experimental observation of fluid flow channels in a single fracture. *J Geophys Res* 103(B3):5125–5132
- Brush DJ, Thomson NR (2003) Fluid flow in synthetic rough-walled fractures: Navier–Stokes, Stokes, and local cubic law simulations. *Water Resour Res* 39(4):1085, doi: 10.1029/2002WR001346
- Cardenas MB, Slottke DT, Ketcham RA, Sharp JM Jr (2007) Navier–Stokes flow and transport simulations using real fractures shows heavy tailing due to eddies. *Geophys Res Lett* 34, L14404, doi: 10.1029/2007GL030545
- Chen Z, Narayan SP, Yang Z, Rahman SS (2000) An experimental investigation of hydraulic behavior of fractures and joints in granitic rock. *Int J Rock Mech Min Sci* 37(7):1061–1071
- Chen Z, Qian J, Luo S, Zhan H (2009) Experimental study of friction factor to groundwater flow in a single rough fracture. *J Hydrodyn* 21(6):820–825
- Eker E, Akin S (2006) Lattice boltzmann simulation of fluid flow in synthetic fractures. *Transp Porous Med* 65:363–384, doi: 10.1007/s11242-005-6085-4
- Esaki T, Du S, Mitani Y, Ikusada K, Jing L (1999) Development of a shear-flow test apparatus and determination of coupled properties for a single rock joint. *Int J Rock Mech Min Sci* 36:641–650
- Frisch U, d'Humières D, Hasslacher B, Lallemand P, Pomeau Y, Rivet JP et al (1987) Lattice gas hydrodynamics in two and three dimensions. *Complex Systems* 1:649–707
- Gao Y, Sharma MM (1994) A LGA model for fluid flow in heterogeneous porous media. *Transp Porous Med* 17(1):1–17
- Giger SB, Clennell MB, Harbers C, Clark P, Ricchetti M, Ter Heege JH, Wassing BBT, Orlic B (2011) Design, operation and validation of a new fluid-sealed direct shear apparatus capable of monitoring fault-related fluid flow to large displacements. *Int J Rock Mech Min Sci* 48:1160–1172
- Gutfraind R, Hansen A (1995) Study of fracture permeability using lattice gas automata. *Transp Porous Med* 18(2):131–149
- Jiang Y, Tanabashi Y, Xiao J, Nagaie K (2004) An improved shear-flow test apparatus and its application to deep underground construction. *Int J Rock Mech Min Sci* 41:385–386
- Kim HM, Inoue J (2003) Analytical approach for anisotropic permeability through a single rough rock joint under shear deformation. *J Geophys Res* 108 (B8):2366, doi: 10.1029/2002JB002283
- Konuk JS, Kueper BH (2004) Evaluation of cubic law based models describing single-phase flow through a rough-walled fracture. *Water Resour Res* 40, W02402, doi: 10.1029/2003WR002356
- Koyama T, Fardin N, Jing L, Stephansson O (2006) Numerical simulation of shear induced flow anisotropy and scale dependent aperture and transmissivity evolutions of fracture replicas. *Int J Rock Mech Min Sci* 43(1):89–106
- Madadi M, Sahimi M (2003) Lattice Boltzmann simulation of fluid flow in fracture networks with rough, self-affine fractures. *Phys Rev E* 67:026309
- Mitsui Y, Iio Y, Fukahata Y (2012) A scenario for the generation process of the 2011 Tohoku earthquake based on dynamic rupture simulation: role of stress concentration and thermal fluid pressurization. *Earth Planets Space* 64(12):1177–1187
- Mourzenko VV, Thovert JF, Adler PM (1995) Permeability of a single fracture: validity of the Reynolds equation. *J Phys II* 5(3):465, doi: 10.1051/jp2:1995133
- Mourzenko VV, Galamay O, Thovert JF, Adler PM (1997) Fracture deformation and influence on permeability. *Phys Rev E* 56(3):3167–3184
- Nicholl MJ, Detwiler RL (2001) Simulation of flow and transport in a single fracture: macroscopic effects of underestimating local head loss. *Geoph Res Lett* 28(23):4355, doi: 10.1029/2001gl013647
- Olsson R, Barton N (2001) An improved model for hydromechanical coupling during shearing of rock joints. *Int J Rock Mech Min Sci* 38(3):317–329
- Oron AP, Berkowitz B (1998) Flow in rock fractures: the local cubic law assumption reexamined. *Water Resour Res* 34(11):2811–2825
- Park JW, Song JJ (2013) Numerical method for the determination of contact areas of a rock joint under normal and shear loads. *Int J Rock Mech Min Sci* 58:8–22
- Piggott AR, Elsworth D (1993) Laboratory assessment of the equivalent apertures of a rock fracture. *Geophys Res Lett* 20(13):1387–1390
- Pot V, Genty A (2007) Dispersion dependence on retardation in a real fracture geometry using lattice-gas cellular automaton. *Adv Water Res* 30:273–283
- Pot V, Karapiperis T (2000) A multi-species lattice-gas automaton model to study passive and reactive tracer migration in 2D fractures. *Eur Phys J B* 13:387–393
- Qian J, Liu Y, Wang J, Guan H, Chen S, Wang J (2006) Non-LCL and tracer test for groundwater flow in a single fracture. *J Hydrodynamics Series B* 18(1):104–108
- Qian J, Chen Z, Zhan H, Guan H (2011a) Experimental study of the effect of roughness and Reynolds number on fluid flow in rough-walled single fractures: a check of local cubic law. *Hydrol Process* 25:614–622, doi: 10.1002/hyp.7849
- Qian J, Zhan H, Chen Z, Ye H (2011b) Experimental study of solute transport under non-Darcian flow condition in a single fracture. *J Hydrol* 399:246–254
- Qian J, Chen Z, Zhan H, Luo S (2011c) Solute transport in a filled single fracture under non-Darcian flow. *Int J Rock Mech Min Sci* 48:132–140
- Qian J, Liang M, Chen Z, Zhan H (2012) Eddy correlations for water flow in a single fracture with abruptly changing aperture. *Hydrol Process* 26:3369–3377, doi: 10.1002/hyp.8332
- Raven KG, Gale JE (1985) Water flow in a natural rock fracture as a function of stress and sample size. *Int J Rock Mech Min Sci* 22(4):251–261
- Tse R, Cruden DM (1979) Estimating joint roughness coefficients. *Int J Rock Mech Min Sci* 16:303–307
- Vilarrasa V, Koyama T, Neretnieks I, Jing L (2011) Shear-induced flow channels in a single rock fracture and their effect on solute transport. *Transp Porous Med* 87:503–523, doi: 10.1007/s11242-010-9698-1
- Watanabe N, Hirano N, Tsuchiya N (2008) Determination of aperture distribution and fluid flow in a rock fracture by high-resolution numerical modeling on the basis of a flow-through experiment under confining pressure. *Water Resour Res* 44, W06412, doi: 10.1029/2006WR005411
- Watanabe N, Hirano N, Tsuchiya N (2009) Diversity of channeling flow in heterogeneous aperture distribution inferred from integrated experimental-numerical analysis on flow through shear fracture in granite. *J Geophys Res* 114, B04208, doi: 10.1029/2008JB005959
- Witherspoon PA, Wang JSY, Iwai K, Gale JE (1980) Validity of cubic law for fluid flow in a deformable rock fracture. *Water Resour Res* 16(6):1016–1024
- Xiong X, Li B, Jiang Y, Koyama T, Zhang C (2011) Experimental and numerical study of the geometrical and hydraulic characteristics of a single rock fracture during shear. *Int J Rock Mech Min Sci* 48:1292–1302

- Yeo IW, Ge S (2005) Applicable range of the Reynolds equation for fluid flow in a rock fracture. *Geosci J* 9(4):347–352
- Yeo IW, De Freitas MH, Zimmerman RW (1998) Effect of shear displacement on the aperture and permeability of a rock fracture. *Int J Rock Mech Min Sci Geomech Abstr* 35(8):1051–1070
- Yu X, Vayssade B (1991) Joint profiles and their roughness parameters. *Int J Rock Mech Min Sct Geomech Abstr* 28(4):333–336
- Zimmerman RW, Bodvarsson GS (1996) Hydraulic conductivity of rock fractures. *Transp Porous Med* 23:1–30
- Zimmerman RW, Chen DW, Cook NGW (1992) The effect of contact area on the permeability of fractures. *J Hydrology* 139(1–4):79–96
- Zimmerman RW, Al-Yaarubi A, Pain CC, Grattoni CA (2004) Non-linear regimes of fluid flow in rock fractures. *Int J Rock Mech Min Sci* 41(3):384, doi: 10.1016/j.ijrmms.2003.12.045

doi:10.1186/1880-5981-66-108

Cite this article as: Nishiyama et al.: Mechanical and hydraulic behavior of a rock fracture under shear deformation. *Earth, Planets and Space* 2014 **66**:108.

Submit your manuscript to a SpringerOpen[®] journal and benefit from:

- Convenient online submission
- Rigorous peer review
- Immediate publication on acceptance
- Open access: articles freely available online
- High visibility within the field
- Retaining the copyright to your article

Submit your next manuscript at ► springeropen.com
